JACS
JOURNAL OF THE AMERICAN CHEMICAL SOCIETY

ARTICLE

pubs.acs.org/JACS

Quantitative Structural Assessment of Heterogeneous Catalysts by Electron Tomography

Roman Grothausmann,*[†] Gerald Zehl,[†] Ingo Manke,[†] Sebastian Fiechter,[†] Peter Bogdanoff,[†] Iris Dorbandt,[†] Andreas Kupsch,[‡] Axel Lange,[‡] Manfred P. Hentschel,[‡] Gerhard Schumacher,[†] and John Banhart[†]

[†]HZB Helmholtz-Zentrum Berlin GmbH, Hahn-Meitner-Platz 1, 14109 Berlin, Germany

[‡]BAM Federal Institute for Materials Research and Testing, 12200 Berlin, Germany

ABSTRACT: We present transmission electron microscope (TEM) tomography investigations of ruthenium-based fuel cell catalyst materials as employed in direct methanol fuel cells (DMFC). The digital three-dimensional representation of the samples not only enables detailed studies on number, size, and shape but also on the local orientation of the ruthenium particles to their support and their freely accessible surface area. The shape analysis shows the ruthenium particles deviate significantly from spherical symmetry which increases their surface to volume ratio. The morphological studies help to understand the structure formation mechanisms during the fabrication as well as the high effectiveness of these catalysts in the oxygen reduction reaction at the cathode side of fuel cells.

1. INTRODUCTION

Platinum catalysts are essential in applications such as fuel cells. Due to the high cost of Pt, replacements are sought. The use of metal nanoparticles finely dispersed on different types of carbon black (with extremely enlarged surfaces) leads to a pronounced reduction of the necessary amount of Pt.[1] To further reduce the costs, Ru as a less expensive and more reliable alternative was suggested as catalyst for the oxygen reduction reaction (ORR) at the cathode side of polymer−electrolyte fuel cells (PEFC).[2−4] Ru-based ORR electrocatalysts modified with selenium even feature a superior methanol tolerance.[5,6] Such systems are of particular interest for direct methanol fuel cells in compact mixed reactant geometry (CMR-DMFC) where methanol tolerance is crucial.[7,8] Intense studies of $RuSe_x$ catalysts have been performed,[7−10] but their ORR activity is still limited to 70% compared to Pt-based reference materials.[9−12]

The optimization of electrocatalysts for oxygen reduction can be brought down to the necessity to tailor a three-phase boundary between the Nafion-phase (supply of H^+), the conductive carbon support (for e^- replenishment), and the catalytically active surface of the transition metal as the center of the catalytic reaction. Hence, there is a soaring interest in characterization techniques capable not only of estimating the overall active surface area of the metallic nanoparticles but also of accounting for particle sizes and shapes, spatial particle distribution and the porosity of the catalyst support.

Information from conventional characterization techniques such as XRD is limited to the average sizes of crystalline particles above 1.5 nm (derived from the Scherrer equation[13]) or to simple size/strain distributions (evaluated by the Warren−Averbach method). Hydrogen and CO chemisorption techniques come to their limits when the stoichiometry is uncertain due to, e.g. the formation of alloyed surfaces or the presence of activity promoters covering an unknown portion of the metallic surface. The electrochemical activity of oxygen reduction catalysts depends to a large extent on the accessible surface area of the metallic nanoparticles and their exposed facets. Conventional TEM is frequently used to characterize nanoparticulate catalysts, and valuable two-dimensional projected structural information can be extracted from these images. Still, a tool to visualize catalytically active nanostructures as virtual three-dimensional (3D) representations easy to perambulate and reliably to evaluate is highly desirable.

Electron tomography represents a powerful characterization technique[14,15] for heterogeneous solid samples.[16−19] Most common are qualitative evaluations[20−22] or manual measurements,[23,24] depending on the personal judgment of the scientist. Recent advances and sophisticated data evaluation extend the field of applications of this technique[25,26] and make it even more attractive for the investigation of heterogeneous catalysts.[27−29] Carbon-supported transition metal catalysts represent a very suited system for such investigations since the contrast between the supporting carbon matrix and the catalytically active metals is sufficiently large.[18,30] The aim of the current contribution is to present a detailed analysis of the size and shape distribution of ruthenium nanoparticles supported on carbon black used as a precursor for the preparation of highly active selenium-modified $RuSe_x$/C ORR-catalysts for the cathode side of PEFCs.[31]

Application of conventional reconstruction algorithms yielded tomograms dominated by artifacts. If at all possible, particle

Received: April 8, 2011
Published: September 14, 2011

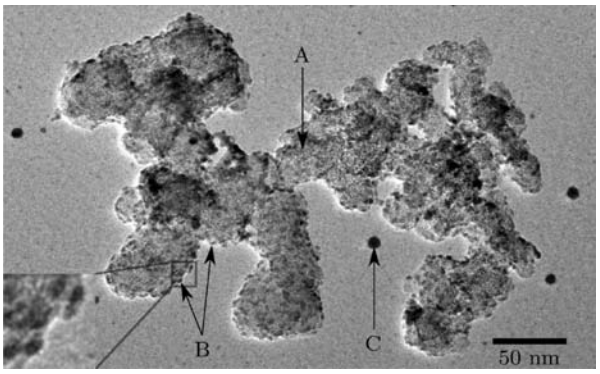

Figure 1. Bright-field TEM image of a catalyst particle showing ruthenium nanoparticles as dark spots supported by a Vulcan XC-72R carbon black agglomerate. To the right of arrow A the C particle is more amorphous, while to the left it has a more graphitic character. Arrows B point at ruthenium particles and arrow C to a fiducial marker for the image alignment.

extraction by appropriate software required a high degree of the operator's personal judgment which can influence results substantially. The novel DIRECTT algorithm[32] increases the reconstruction quality (in particular regarding the spatial resolution and the absolute contrast scale) tremendously so that the need of image postprocessing (filtering) was reduced to a minimum.

New software was developed to create a set of tools to automate the process of evaluating thousands of particles. These programs have been designed with a special emphasis on bringing down the image analysis parameters to very basic properties of the measurements to minimize the possible influence of personal judgment in the analysis. A reliable evaluation of the 3D structure of the catalyst and of the size and shape distribution of ruthenium on the carbon support contributes to the understanding of the fundamental chemical and physical processes that make these types of catalysts so effective.

2. EXPERIMENTAL SECTION

2.1. Sample Preparation. The commercially available carbon black Vulcan XC-72R obtained from Cabot Corporation[33] was used as starting material to prepare carbon-supported ruthenium nanoparticles. Vulcan XC-72R represents an industrial standard for conductive carbon blacks and is therefore widely used as a common catalyst support for fuel cells. The specific surface area determined by the BET-method (Brunauer, Emmett, Teller[34]) is about 230 m^2/g. The specific pore volume evaluated with the BJH-method (Barrett, Joyner, Halenda[35]) (incorporating volumes between carbon particles) is 0.62 cm^3/g and 0.066 cm^3/g with the *t*-plot method[36] (only regarding mesopores but not micropores). $RuCl_3 \cdot xH_2O$ (Sigma-Aldrich, metal content 35 wt %) was used as Ru precursor for catalyst preparation (100 mg Vulcan and 71 mg $RuCl_3$ in 200 mL H_2O). All solvents were dried over molecular sieves before precursor solutions of appropriate Ru concentration were prepared. $RuCl_3$ was dissolved in water that had been purged with argon before. The precursor solutions were placed in a round-bottom flask at the end of a quartz tube which was inserted into a split-hinge tube furnace. The resulting suspensions were agitated by ultrasound, after which the solvent was removed by rotary evaporation, and the dried catalyst powder was heated under hydrogen at a temperature of 200 °C for 30 min. The resultant material was rinsed with water to remove all chlorine-containing residues and was finally dried in a desiccator. The investigated carbon-black supported ruthenium particles were prepared as described in ref 37. For the preparation of samples suitable for electron tomography, this coarse powder was dispersed in butanol by ultrasound. The dispersion was then dropped onto a copper grid with a thin carbon foil containing fiducial gold markers (Figure 1) and dried in a furnace to remove remnants of the butanol.

2.2. Data Acquisition and Procession. Electron tomography experiments were performed with a Zeiss LIBRA 200FE transmission electron microscope (TEM) at the Helmholtz Centre Berlin (HZB). Bright-field images were taken at 200 keV while the sample was tilted from −69° to +74° with an angular increment of 1°. *x*−*y*−*z*-tracking[38,39] was done by the Digital Micrograph tomography module (Gatan). The images were aligned by fiducial marker tracking using the software IMOD,[40] which revealed that the actual angles of projections differed from the nominal angles as much as 0.2°. Thus, tomographic reconstruction suffers from various limitations (i.e., deviations from ideal complete tomographic data): a limited range of tilt angles, too few projections with respect to the detector size of 2048 × 2048 pixels, partial opacity caused by some of the gold markers, a nonequidistant set of angles, and a problem of the influence of object parts outside the region-of-interest. Conventional reconstruction software does not account well for all these restrictions, but the DIRECTT algorithm (direct iterative reconstruction of computed tomography trajectories[32,41]) proved to perform excellently under these conditions. DIRECTT represents a promising alternative to conventional algorithms such as WBP (weighted back projection) or SIRT (simultaneous iterative reconstruction technique). Instead of back-projecting all sinogram values at once, it traces single sinusoidal trajectories in Radon space which are selected from the set of all possible trajectories by criteria such as their angular averaged (filtered) weight or contrast to adjacent trajectories. These reconstruction elements are only partially added to an intermediate reconstruction. The projection (Radon transform) of this reconstruction is subtracted from the original (i.e., measured) data set in a next step. The obtained residual sinogram is treated in the same way as in the subsequent iteration steps until a preselected criterion of convergence is reached. Data preprocessing combined with the advantages of DIRECTT, in particular, extending the reconstruction region beyond that given by the input image size,[42] proved to effectively eliminate disturbing streak artifacts.

In the resulting tomogram, each voxel value (gray value) corresponds to the local attenuation coefficient of the specific elements or phases. Each element present in the sample can be assigned to a segment of the tomogram with two appropriate thresholds on the gray values. This step is called 'segmentation' and each segment represents a binarization of the tomogram (e.g., bottom images of Figure 2).

The ruthenium segment was created by applying the Otsu-threshold[a] criterion.[43] Therefore, decisions by the operator were not required. Computer analysis of the binarized tomogram segments enabled global measurements concerning ruthenium and carbon and also measurements of each individual ruthenium particle. The digital analysis was carried out with the Insight Toolkit[44] (ITK), the Visualization Toolkit[45] (VTK), octave,[46] gnuplot,[47] and rendered with Blender.[48]

Although the reconstructions have few artifacts, some ruthenium particles, that are very close to each other, are connected because of limited spatial resolution. Therefore, the particles were separated by applying successively two distance map evaluations and a watershed transformation.[49,50] The dependence on the second distance map was introduced to control over- and under-segmentation by ascertained separation and edge uncertainties. The result is more realistic concerning number, size, and shape of the ruthenium particles with respect to the original TEM images.

3. RESULTS

We describe the general properties of the catalyst particles in section 3.1. The global measurements of the ruthenium and the

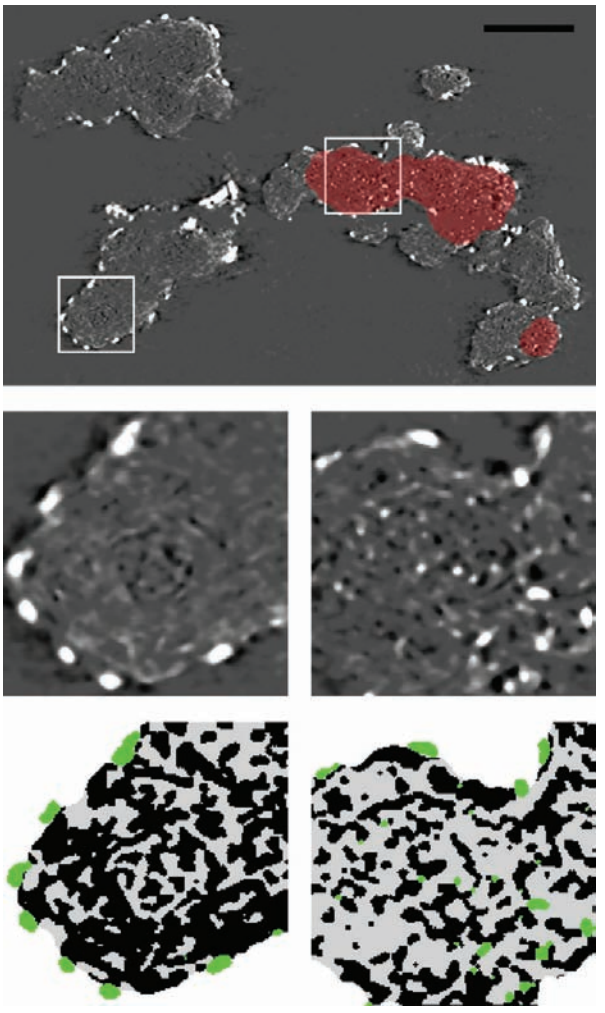

Figure 2. Cross section through the reconstructed tomogram. The upper image shows a cross section through the whole tomogram (contrast-inverted, scale bar 60 nm); red marks the regions that have a more amorphous-like carbon structure; the remaining carbon has a more graphitic character. The middle images show the framed regions of the two different structures in magnification. The result of the segmentation (before watershed separation) is shown in the bottom images.

carbon segments are presented in section 3.2, followed by an evaluation of the sphericity of the ruthenium particles (section 3.3), showing to which extent a size distribution under the assumption of spherical symmetry (section 3.4) makes sense, motivating further investigations of shape by fitting of ellipsoids (sections 3.5 and 3.6). The size distribution (although most particles are not spherical [see Figures 1 and 2]) allows comparison of the results with those from other methods such as X-ray diffraction (XRD) and anomalous small-angle X-ray scattering (ASAXS) (section 4) which were based on spherical approximations. After the evaluation of the shapes of the ruthenium particles, the analysis is extended to the local carbon morphology in the vicinity of each ruthenium particle (sections 3.6−3.8).

3.1. Visual Assessment and 3D Reconstruction. Figure 1 shows a bright-field TEM image of ruthenium catalyst nanoparticles (small dark spots) distributed over an agglomerate of Vulcan XC-72 carbon black support (arrow A) deposited on a carbon foil. The carbon particle in Figure 1 consists mainly of two fractions differing by their appearance and degree of graphitization. Most carbon particles are polycrystalline. As 'degree of graphitization' we designate the fraction of graphitic regions in an otherwise amorphous carbon particle. According to ref 51, the structural properties of graphitic crystals are described adequately by crystallite size, crystallite dimension in the *a*- and *c*-axes direction, and the interlayer spacing. Although the model in Figure 2 of ref 51 shows well-defined monocrystalline regions, the transition from graphitic to amorphous carbon is continuous (see, e.g. Figure 3 of ref 51). Therefore, the listed properties are not easily determined. Hence, we use the terms 'more amorphous' and 'more graphitic' to express the tendency of the local carbon structure. The tendency toward more graphitic carbon structure is expressed by a higher ordering of the graphene sheets and a more ball-shaped structure, creating the impression of onion layers.

In Figure 1, larger branches of an onion-like structure with diameters of around 50 nm (mostly on the left side of arrow A) are combined with smaller amorphous-like constituents forming irregular aggregates that vary from 10 to 30 nm in width (mostly on the right side of arrow A). The much smaller ruthenium particles range from 1 to 5 nm in size (see arrows B and inset) and are spread over the surface of the carbon support. Fiducial gold markers are visible as separate spherical dots on the support foil (arrow C) and were used for image alignment.

Figure 2 shows a cross section through the median-filtered and segmented tomogram of the sample. The complete tomographic data set consists of many such slices covering the whole reconstructed volume. Most of the ruthenium particles are located on the outer surface of the carbon support and are partially embedded. This is typical for onion-like structured carbon regions. Some ruthenium particles can also be found inside the carbon matrix (see images on the right in Figure 2). These particles are much smaller than those on the surface. However, they can only be found at some locations. This observation is further evaluated in section 3.7.

3.2. Volume and Surface Measures of Carbon and Ruthenium Segments. The different materials (gray values) of the tomogram (see Figure 2) are assigned to different segments for further investigations. A cross section through the tomogram segments after removal of reconstruction artifacts is shown in the bottom images of Figure 2: carbon segment (black), ruthenium segment (green), the pore segment (diameter less than 5 nm, gray), and the surrounding empty space (white) of the tomogram.

The Carbon Segment. Carbon soot usually used as conductive and inert support for catalytically active metallic nanoparticles is a highly porous material. Since the contrast between carbon and the surrounding empty space is not high and the pores within the carbon matrix can be very small, the representation of the pores is less accurate than the representation of the outer contour of the carbon support.

Voids inside the carbon matrix with wall distances of less than 5 nm were treated as 'pores'. A morphological closing operation[50] was applied to the carbon segment to create a carbon representation without pores. Three small voids inside the carbon are left after the closing operation. More important, the outer surface remains largely unchanged. These two representations enable us to discriminate between outer and inner surface of the carbon structure. On this basis, the carbon support particle in Figure 1 has a volume of $V_{op} \approx 10.8 \times 10^5$ nm^3 (volume with open pores) and a total surface area of $S_{op} \approx 12.3 \times 10^5$ nm^2. The closing operation increased the volume by 52% to $V_{cp} \approx 16.4 \times 10^5$ nm^3 (volume with closed pores) while the surface decreased

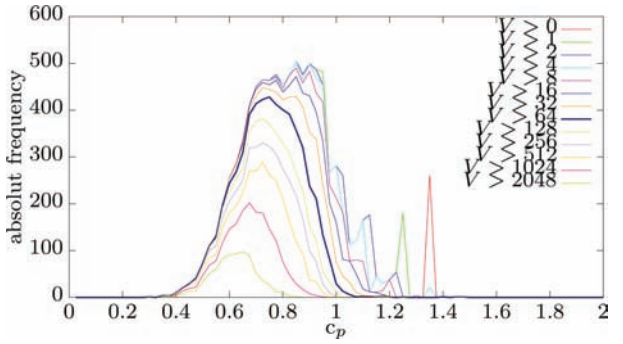

Figure 3. Sphericity of the ruthenium particles. Histogram plots of the sphericity c_p of the ruthenium particles. Only particles whose volume (in voxels) was larger than the chosen threshold were considered in the corresponding histogram.

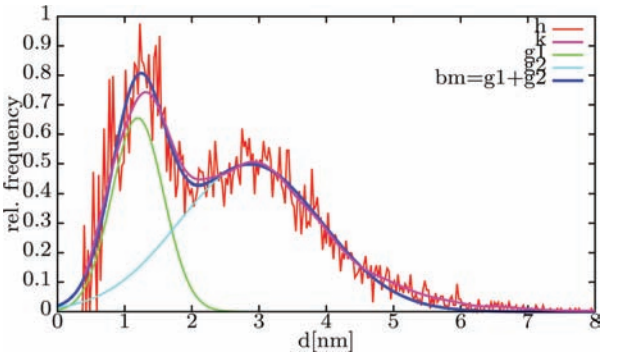

Figure 4. Ruthenium particle size distribution. Histogram showing the distribution of the diameters of all representative ruthenium particles assumed to be spherical.

to $S_{cp} \approx 2.69 \times 10^5$ nm^2. The pore volume then is: $V_p = V_{cp} - V_{op} \approx 5.6 \times 10^5$ nm^3; and the corresponding pore surface: $S_p = S_{op} - S_{cp} \approx 9.61 \times 10^5$ nm^2. The ratio of the inner surface to the outer surface is $S_p/S_{cp} \approx 3.6$, and the surface-to-volume ratios are: $S_{op}/V_{op} \approx 1.14$ nm^{-1}; $S_{cp}/V_{cp} \approx 0.16$ nm^{-1}. These values are a measure of the surface roughness of the carbon support. The larger the roughness, the more sites there are for ruthenium particles to grow. The less carbon volume that is necessary for this, the better the packing of the whole structure with ruthenium particles. However, a very high packing would be counterproductive since then the ruthenium particles are less likely to be reached by the reactants during catalysis.

The specific surface area of the carbon deduced from these values, $S_s = S/\rho_C/V$, lies between 100 m^2/g and 500 m^2/g, and the specific pore volume, at around $V_s = V_p/\rho_C/V_{op} \approx 0.23$ cm^3/g.[c]

The Ruthenium Segment. Before separation (see section 2.2, denoted: bs), there are about 2600 particles with a particle volume of at least 64 voxels ≈ 1.12 nm^3. The total Ru volume is $V_{bs} \approx 1.1 \times 10^5$ nm^3, and the surface, $S_{bs} \approx 2.03 \times 10^5$ nm^2.

The ruthenium surface not covered by carbon is evaluated by slightly dilating the carbon representation, followed by a conversion of both segments into a mesh representation (see section 3.8). Now the triangles of the ruthenium surface mesh that do not reside inside the dilated carbon support are regarded as 'uncovered ruthenium surface' (denoted ubs: uncovered, before separation) and is $S_{ubs} \approx 0.74 \times 10^5$ nm^2, which is about 36% of the total ruthenium surface S_{bs}. This ratio of uncovered ruthenium surface to total ruthenium surface (Σ) is a key quantity for the effectiveness of the catalyst and will be further discussed in section 4.

After separation (denoted as), there are about 5700 particles (again $V > 64$ voxels) and a total ruthenium volume of $V_{as} \approx 1.1 \times 10^5$ nm^3. Since no voxels are removed by the watershed algorithm chosen, the overall ruthenium volume is not changed. The surface, however, is increased by 11% to $S_{as} \approx 2.25 \times 10^5$ nm^2 due to the boundary surface introduced. It is unclear though if this additional surface area is real. Even if, its contribution to catalysis would probably be insignificant because the distance to the nearby particles is too small to allow for good accessibility of this additional surface by the reactants. Therefore, in addition to Σ, we use S_{bs} and S_{ubs} for the calculation of the following values, which we think are important for a comparison with other catalysts of similar type:

- Γ: The amount of uncovered ruthenium surface per unit support surface characterizes the degree of utilization of available support surface.
- Θ: The amount of uncovered ruthenium surface per unit Ru/C catalyst volume can be used for the evaluation of space needed when loading the cathode up to a specific catalytic active surface.
- Ξ: The amount of uncovered ruthenium surface related to the mass of the Ru/C catalyst is a more convenient measure when preparing materials for catalyst production.[b]

For the presented sample:

$$\Sigma = S_{ubs}/S_{bs} = 36\% \text{(defined before)}$$

$$\Gamma = S_{ubs}/S_{op} = 6\%$$

$$\Theta = S_{ubs}/(V_{cp} + V_{bs}) = 0.04 \text{ nm}^{-1}$$

$$\Xi = S_{ubs}/(\rho_C V_{op} + \rho_{Ru} V_{bs}) = 0.02 \text{ nm}^2/g^c$$

3.3. Deviation from Spherical Symmetry. Most ruthenium particles deviate from spherical shape (see inset in Figure 1 and Figure 2). To quantify this, the sphericity $c_p = 6(\pi)^{1/2}V/S^{3/2}$ of the ruthenium particles was investigated. For a sphere $c_p = 1$, for any other shape $c_p < 1$.

Figure 3 shows multiple histograms of the sphericity. The histograms differ by their minimum volume threshold. Particles with volumes below this threshold are not included in the corresponding histogram. Values above 1 are caused by errors in the surface estimation of the small particles (see, for example, ref 53). Such particles have to be neglected. Therefore, we restrict our further analysis to particle volumes above 64 voxels.

For any histogram in Figure 3 with a minimum volume threshold of at least 64 voxels, there are very few particles that are actually spherical ($c_p = 1$). The degree of deviation from spherical shape is much more pronounced than expected from conventional 2D TEM images and as commonly assumed for such metallic nanocrystallites.[5] This suggests fitting ellipsoids to the ruthenium particles rather than simple spheres. Generally, it can be assumed that the particles have the form of truncated hexagonal bipyramids because Ru metal crystallizes in a hexagonal closed-packed structure.[54] However, the truncated bipyramids are expected to resemble shapes close to ellipsoids if the

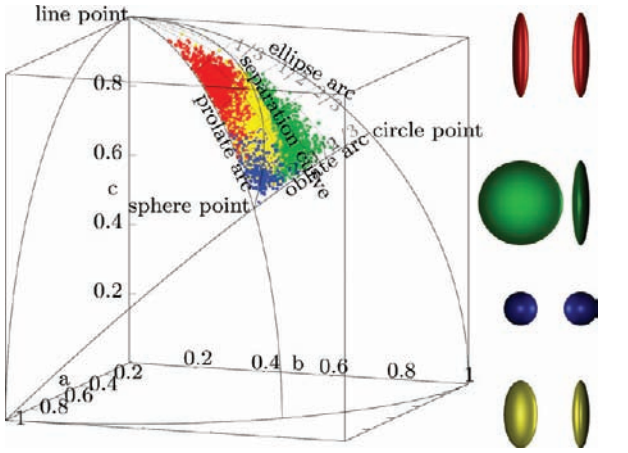

Figure 5. Radial projection of the end-points of the point vectors of all *a*:*b*:*c*-ratios onto the unit sphere. The ellipsoids on the side represent the four different types in their extremes (second column: view rotated by 90°).

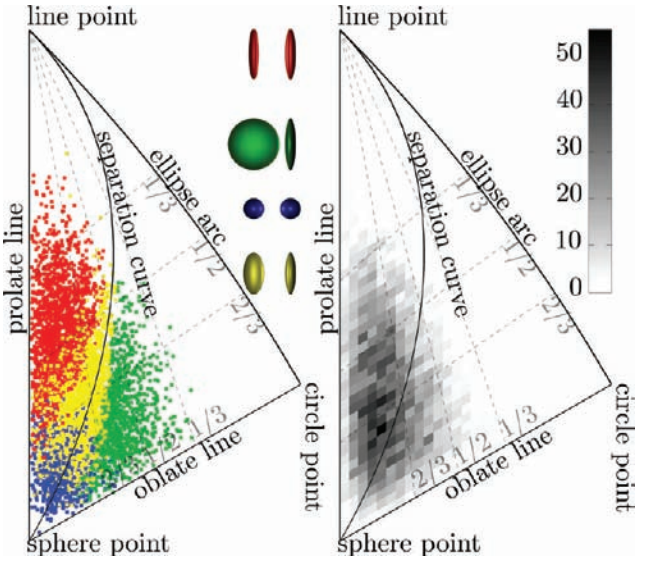

Figure 6. Stereographic projection of *a*:*b*:*c*-ratios and 2D-histogram. (a) Stereographic projection of Figure 5. (b) Two-dimensional histogram showing the distribution of the *a*:*b*:*c*-ratios.

resolution of the tomographic data set is insufficient to reveal facets. The shape of the resulting particle representations can range from prolate (cigar-shaped) to oblate (lentil-shaped) depending on the position of the truncation or preferential growth directions. The additional information of the ellipsoid fitting allows estimation of the significance of these influences.

3.4. Ruthenium Particle Size Distribution. The size distribution of the ruthenium particles (Figure 4) is given as a function of the diameter of a sphere with the same volume as the corresponding particle. The normalized histogram (h) has 300 bins and shows a noisy but distinct bimodal distribution of the particle diameters (particles with $c_p > 1$ were excluded). A kernel density (additive Gaussian functions) distribution plot (k) accounts for the uncertainty of the representation of ruthenium particles. This also reduces the noise, and the bimodal distribution becomes more obvious. The distribution was decomposed into two Gaussian functions $g1$ and $g2$ centered at d_1 = 1.2 nm (variance 0.4 nm) and d_2 = 2.8 nm (variance 1.0 nm).

3.5. Shape Analysis. Shape analysis is realized by fitting an ellipsoid to each particle after watershed separation. The parameters of the ellipsoid (axes lengths and axes orientations, position in space) are determined by the binary image moments.[55,56] The fitted ellipsoids were scaled to have the same volume as the corresponding particles since this does not change the ratio of the lengths of the main axes: *a*:*b*:*c* (*a*:*b*:*c*-ratio from now on).

These *a*:*b*:*c*-ratios can be regarded as point vectors in 3D space. However, for the evaluation of the shape of each particle, its actual size, i.e. the actual length of the point vector, is of no importance. Therefore, all data points were radially projected onto the unit sphere, as displayed in Figure 5.

We sorted the axes by their lengths $a < b < c$ which makes the naming distinct. This causes the points to be restricted to a rectangular spherical triangle on 1/48 (1/8·1/6, for symmetry reasons) of the unit sphere. The points on the triangle arcs correspond to special ellipsoids:

prolate arc: $a = b < c \Leftrightarrow 1 = a/b < c/b$
oblate arc: $a < b = c \Leftrightarrow a/b < c/b = 1$
ellipse arc: $a = 0$

The naming of the axes does not correspond to the common naming in hexagonal systems. Prolate ellipsoids (cigar shape) have a rotational symmetry about the long axis (c), whereas the oblate ellipsoids (lentil shape) have a rotational symmetry about the small axis (a). The corner points of the spherical triangle in Figure 5 correspond to even more special conditions of the ellipsoids:

sphere point: $a = b = c$
circle point: $a = 0 \wedge b = c$
line point: $a = b = 0$

Exact prolate, oblate, and spherical ellipsoids, i.e. with rotational symmetry, solely represent extreme geometrical cases that are unlikely to appear in reality. A large fraction of data points is mapped within significant distance away from the sphere point, indicating that the majority of particles are nonspherical in accordance to the results of section 3.3.

A way to partition all possible ellipsoids into two definite classes is to define the separation condition $a/b = b/c$. Ellipsoids with $a/b < b/c$ are oblate-like, whereas those with $a/b > b/c$ are prolate-like. The condition $a/b = b/c$ corresponds to the case where the eccentricity of the ellipse in the $a-b$-plane equals the eccentricity of the ellipse in the $b-c$-plane. This defines the separation curve in Figure 5.

Each *a*:*b*:*c*-ratio has an error because of the uncertainty in the particle representation. This can be regarded as an error box (not shown) around each point in Figure 5. If the error permits the shape to be either prolate or oblate (i.e., the error box intersects with the separation curve), the shape is uncertain within the error limits. If, however, the error box includes the sphere point, the ellipsoid can be regarded as spherical within the error limits.

In Figure 5 the color of each point corresponds to its ellipsoid type: prolate: red (1783); oblate: green (983); spherical (within error limits, 676): blue; uncertain (within error limits, 2257): yellow. The broken lines ending at the oblate arc mark the corresponding a/b-ratios; those ending on the ellipse arc mark the corresponding b/c-ratios.

This spherical triangle is stereographically[d] projected (Figure 6a). The origin of projection was chosen to be the 'sphere point' such that the prolate and the oblate arcs from Figure 5 are projected onto straight lines.

The true point density cannot be read from Figure 6a due to overlap of points. The 2D histogram in Figure 6b visualizes the

dx.doi.org/10.1021/ja2032508 |J. Am. Chem. Soc. 2011, 133, 18161–18171

Figure 7. Spatial distribution of the fitted ellipsoids. Green: oblate, red: prolate, yellow: indistinguishable, blue: spherical within the error limits. The particle density is higher on the right side.

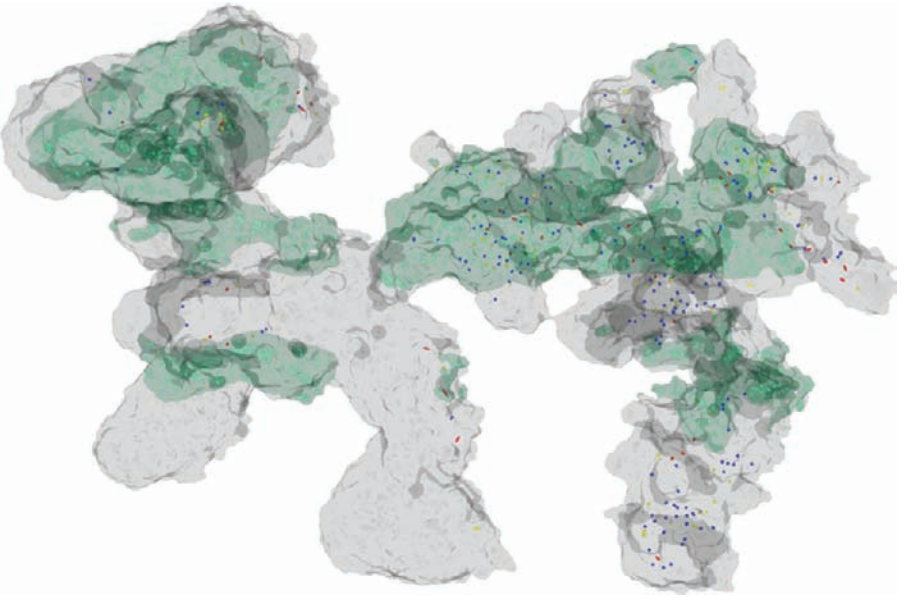

Figure 8. Relation of the inner ruthenium particles to the carbon support. The image shows only the small ellipsoids that are inside the outer carbon surface (gray). Most of the small inner ellipsoids are spherical (blue) and are located in the right side of the support. The light green surfaces enclose regions of the carbon particle with a higher local pore density. These surfaces originate from the thresholded results of the local pore density filter (lpd_{16}) described in section 3.7.

actual point density distribution of *a*:*b*:*c*-ratios. The gray scale indicates the amount of *a*:*b*:*c*-ratio-points within a field, i.e. the number of particles whose a:b:c-ratios are similar. The fields are not rectangular to avoid underestimation along the 'oblate line'. It is visible that the prolate-like ellipsoids dominate over the oblate-like ones, since the densities in Figure 6b are higher in the prolate region (red points in Figure 6a) than in the oblate region (green points in Figure 6a).

3.6. Spatial Distribution of Ruthenium Particles. We investigated how the studied particles of different shapes are distributed in space. For this, each ellipsoid is displayed at the centroid (barycenter or center of 'mass') of the corresponding particle (Figure 7).

Most of the spherical ellipsoids (blue) are small (Figure 7) and are located inside (Figure 8) the carbon support particle where the carbon seems to be predominantly amorphous (see Figures 1 and 2). Limited spatial resolution can be a reason for some small particles to appear spherical. However, many other small particles, especially those located on the surface of the carbon support, have a distinct ellipsoidal shape despite their small volume.

This was further evaluated by removing the ellipsoids that are bigger than 2.2 nm^3 (128 voxel), which corresponds to a diameter exceeding 1.6 nm, close to the intersection of the two Gaussian functions in Figure 4. Additionally, ellipsoids within a

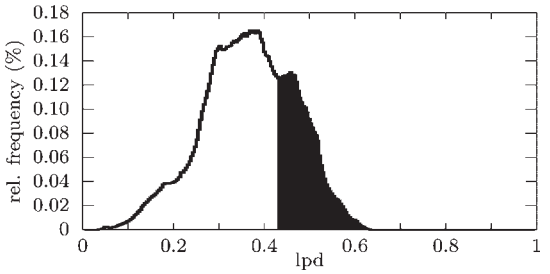

Figure 9. Histogram of the local pore density (lpd_{16}). This lpd_{16} is the local ratio (within a spherical vicinity of 16 nm radius) of the pore volume (pores below 5 nm diameter) to the sum of the pore volume and the carbon volume.

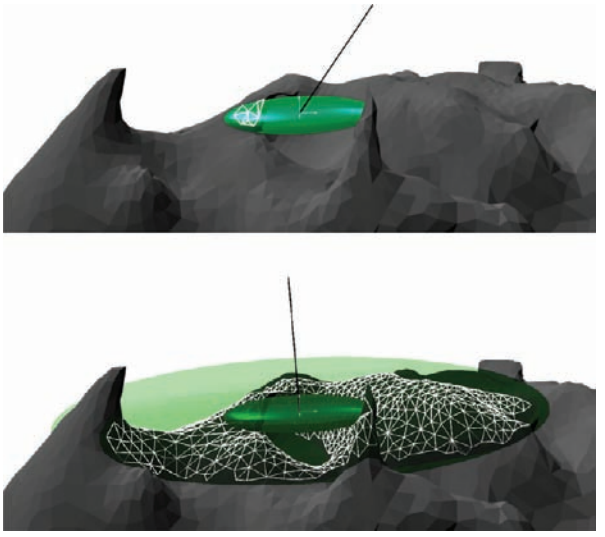

Figure 10. Determination of a local surface normal of the carbon support (schematic). (Upper image) A fitted ellipsoid representing a nonspherical ruthenium particle on the surface of the carbon support and the local carbon surface normal (black line). (Lower image) The ellipsoid and an up-scaled one (transparent). The triangles contributing to the surface normal calculation increased significantly yielding a more appropriate estimation of the average surface normal.

5 nm (20 voxel) vicinity of the nonporous representation of the carbon support (gray surface in Figure 8) were removed as well. Figure 8 shows that the remaining ellipsoids dominate the right part of the carbon particle which is also the part identified as more amorphous-like by TEM (Figure 1).

3.7. Local Pore Density of the Carbon Support. We analyzed the correlation between the density of ruthenium particles inside the carbon support and the apparent carbon structure (crystalline/amorphous) more quantitatively. The approach to distinguish between the two forms makes use of their apparent different porous structure. For each voxel, a local pore density (lpd) was calculated, which is the ratio of the pore volume (pores below 5.2 nm diameter, see bottom images of Figure 2) to the sum of the pore volume and the carbon volume (disregarding the outside space) within a vicinity sphere of radius R_v around each voxel.

For a vicinity of $R_v \approx 16$ nm, the corresponding lpd_{16} shows a bimodal distribution (Figure 9). The regions in the tomogram with $lpd_{16} > 0.43$ (black histogram part) were enclosed by a green

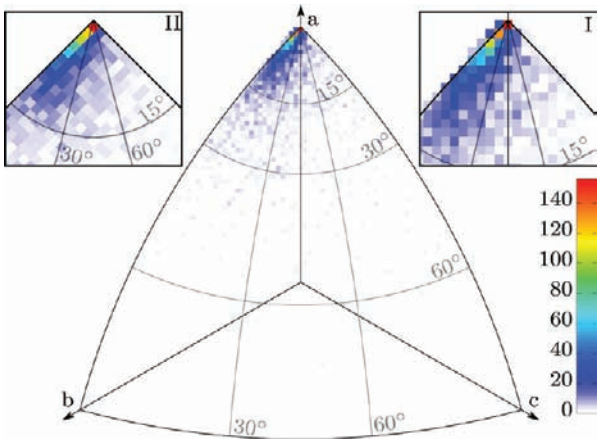

Figure 11. Tendency of the ellipsoids to orient along the local support surface. Inlays I and II show the region around the *a*-axis magnified by two. As most points are close (up to 15°) to the *a*-axis [100], it is sensible to project stereographically along [100] (Inlay II). This allows circumventing the under sampling of the histogram fields along the edges.

surface mesh in Figure 8. These are the regions which correspond to highly porous parts of the carbon particle.

The regions on the right can be assigned to the predominantly amorphous parts which have been identified in sec 3.1. However, on the left, there is also a region with a high lpd_{16}. This is because the more graphite-like carbon parts can also contain voids in the shape of bent plates between 'onion layers' which dominate the left side of the carbon particle (Figure 2).

3.8. Orientation of the Ruthenium Particles on the Carbon Surface. The fitted ellipsoids not only allow for an evaluation of the particle shape but also for an analysis of the orientation of the ruthenium particles with respect to the carbon support. This can be quantified by the orientation of the mean local surface normal of the carbon support relative to the ellipsoid axes. The voxel representation of the carbon support particle has to be converted to a surface mesh to derive a mean local surface normal. The discrete-marching-cubes algorithm[45,57] in combination with a windowed-sinc-smoothing filter[45,58] was used to create such a mesh representation of the carbon support surface consisting only of triangles. Figure 10 demonstrates this approach. For the estimation of the local mean normal, the vector sum of triangle normals weighted by their triangle area is calculated. The summation is over all surface triangles of the carbon support that reside inside the ellipsoid. The triangles of the carbon mesh inside the ellipsoid are highlighted in Figure 10. The direction of the mean surface normal is indicated by the line originating from the center of the ellipsoid. Note that triangles not visible in Figure 10 also contribute to the normal calculation.

The upper image in Figure 10 shows that this estimation can be inappropriate if the ellipsoid only encloses very few triangles of the carbon surface. The ellipsoid was inflated by about 1 nm in all directions to improve the estimation (see lower image in Figure 10). After this inflation, many more triangles are considered in the calculation of the mean local carbon surface normal. It only makes sense to consider ellipsoids near the carbon surface, i.e. that intersect with the smoothed mesh of the carbon surface.

Finally, the orientation of the local surface normal relative to the axes of the ellipsoid can be evaluated. A graphical visualization of these results can be obtained by regarding the orientation

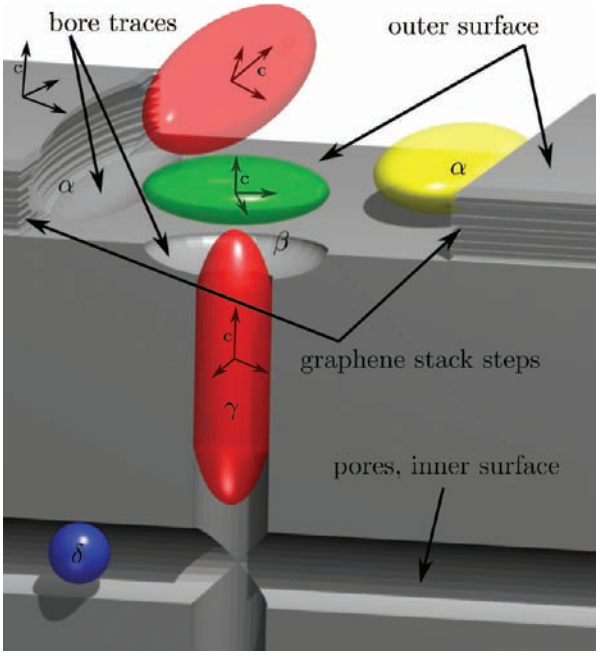

Figure 12. Schematic image of the ruthenium particle positions. Schematic cut-out of the structure to visualize the idealized positions of ruthenium particles related to features of the carbon support. Ruthenium particles are represented by their most likely type of fit-ellipsoid colored according to Figure 6. The particle positions at a step of a stack of graphene layers is marked by α. Pores can be closed (position β) by oblate or prolate particles or a combination of the two types. Particles inside pores close to the outer surface (position γ) can grow until their shape is restricted by the pore. Particle positions deep inside the pore system are denoted by δ. Two ellipsoids are slightly lifted from the surface to reveal their embedding/bore traces in the carbon. Local *crystallographic* coordinate systems are drawn for some ruthenium particles and graphite.

of the local surface normal as a point on the unit sphere. The coordinate system implied by the ellipsoid's axes can be chosen such that all angles are $\leq 90°$. This makes the points of all local normals lie within the spherical triangle of the first quadrant and allows combining the data in a single plot. Figure 11 shows the stereographic projection (along [111]) of this quadrant. As before, the point density is visualized by a 2D-histogram. The corners of the projected spherical triangle correspond to the directions of the ellipsoid axes.

Most particles are oriented in such a way that the local surface normals of the carbon support point along the *a*-axis which is by definition the smallest of the ellipsoid's axes. As a preliminary conclusion, this means that most particles stick to the carbon in such a way that they are in a potential minimum of the attractive forces of the carbon surface, i.e. they stick to the carbon support with their least curved ('flattest') side. For a nearly even surface this also means that the contact area of the slightly embedded particles to the carbon surface is maximized, as generally expected.

However, the 2D-histogram in Figure 11 shows a significant deviation from the expected radial distribution around the *a*-axis point in the top corner. A larger fraction of particles can be found along the arc connecting the *a*-axis and the *b*-axis (see inset II in Figure 11). This suggests that a statistically significant number of particles not only contact the carbon support with their largest side but also with the next smaller side. Such cases can be explained by particles aligned along steps of graphene layers on the outer surface of the carbon support (as will be explained in Figure 12).

4. DISCUSSION

The presented methods provide a very detailed insight into the morphology of the samples studied and allow drawing conclusions about important processes taking place not only during production but also during catalysis. The methods of digital image analysis developed are not restricted to TEM tomography but could also be applied to any 3D tomographic data set, e.g. that dobtained by X-ray tomography.

Carbon-supported ruthenium nanoparticles may be used to catalyze the oxygen reduction reaction at the cathode side of fuel cells. However, their catalytic activity for this reaction can be significantly enhanced by decorating the surface of the ruthenium particles with Se. This yields a catalyst with commercial significance. As the structure predetermined by Ru/C can be analyzed unambiguously by TEM tomography, the results should also be valid for $RuSe_x$/C catalysts since selenization does not alter the material's morphology above the resolution limit of TEM tomography.[5] Thus, we used a Se-free Ru/C intermediate which represents the final morphology despite the simplification.

Neutron activation analysis (NAA) yields a mass ratio of ruthenium to carbon of $m_{Ru}/m_C = 20.6\%$. This is equivalent to a volume ratio[e] of V_{Ru}/V_C ranging from 3.3% to 4.2%; the same ratio evaluated from the tomogram ranges from 3.7% to 28% (determined by erosion and dilation of the segments).

The specific surface area of the used carbon evaluated by the BET-method (230 m^2/g) lies within the range determined by electron tomography (S_s ranging from 100 m^2/g to 500 m^2/g). Values for the specific surface area of Vulcan reported in literature range from around 100 to 300 m^2/g.[59] The higher limit for S_s derived from electron tomography is reasonable taking into account that Vulcan carbon particles exhibit also highly porous parts (see section 3.7) which are comparable to 'Black Perl' carbon (whose specific surface area reaches up to about 1500 m^2/g[59]). Depending on the amount of highly porous regions within a carbon particle, the value for S_s determined by electron tomography will vary in regard to that of integral methods such as BET.

The specific pore volume evaluated by the BJH-method (0.62 cm^3/g) also incorporates volumes between carbon particles whereas the *t*-plot method (0.066 cm^3/g) only regards mesopores but not micropores. The specific pore volume derived from electron tomography ($V_s \approx 0.23$ cm^3/g) lies in between because only pores below 5 nm including micropores are regarded.

TEM tomography shows that most ruthenium particles are formed on the outer surface of the carbon support particles. The carbon support has different structures within it, one is more amorphous and the other more graphitic in character. These two carbon structures affect the formation of the ruthenium particles. The ruthenium particles have a preference to grow on the outer surface, but in the amorphous parts small ruthenium particles also exist inside the support.

Most ruthenium particles are found on the outer surface although the inner surface is about 3.6 times larger than the outer surface. This is due to the limited or restricted supply of $RuCl_3$ during the formation process of the ruthenium particles: $RuCl_3$ solution can penetrate deep into the pore system of the

amorphous carbon because it has shorter and more direct connections to the outer surface (see Figure 2). The pores found in this region are comparable with types (c), (d), and (e), sketched in the schematic cross section in Figure 1 of ref 60. The pores or cavities (like type (a) in ref 60) in the more graphitic regions (the regions that are like layers of onions) have little or no direct connections to the outer surface which prevents the $RuCl_3$ solution from penetrating deep into this pore system.

Supply of $RuCl_3$ solution is important for the formation of ruthenium particles. If the supply in the pores is limited or even ceases, because the connection to the $RuCl_3$ reservoir is blocked by precipitation of the liquid close to the entries of micropores, the number of ruthenium particles formed after hydrogen treatment is limited and the particle shape is then defined by the size and the geometry of the micropore (see Figure 12). Therefore, the particles that form inside the pore system (blue ellipsoid in Figure 12) cannot grow as much as the particles on the outer surface. Furthermore, only very few particles can grow in the more graphitic regions since the pore system here has even fewer connections to the outer $RuCl_3$ supply. This explains why only very few ruthenium particles are inside the part left of arrow A (Figure 1) despite the high *lpd*, but also why the ruthenium particles in the more amorphous part on the right are small.

Hence, the large inner surface of the carbon support contains fewer ruthenium particles than the outer surface and therefore the inner surface and its ruthenium particles contribute less to the overall catalytic effectiveness of the material. In other words, the increase of the surface-to-volume ratio by the inner surface (from 0.16 nm^{-1} to 1.14 nm^{-1}) has less effect than an increase of the ratio by additional outer surface would have. Space in the pores is too restricted (i.e., the pore volume is too small) for the pore system to have the same importance on catalysis as the outer structure. This holds with respect to the amount of catalytic sites but also regarding the accessibility of these sites by the reactants.

One third of the total ruthenium surface has no interface with the carbon support. One explanation for this low amount is the confinement of the particles inside the pores and the partial embedding of the outer particles into the carbon support (see Figure 12). This means that only one-third of the total surface of the ruthenium particles present in the investigated sample can contribute to the catalytic active surface in the process of the oxygen reduction reaction at the cathode side in a fuel cell. This result can tentatively be explained by particle formation as a result of the interaction of the $RuCl_3$ precursor adsorbed on the carbon surface and the subsequent reduction of it by hydrogen. Nucleation of metal particles is most likely to take place in pores and along steps/kink sites of graphene layers at the outer surface of the carbon support. Homogeneous nucleation can be expected in amorphous cavities of the carbon support. Formation of (001), (100), (011) and facets of equivalent symmetry is most likely due to their low surface energies.[54] These crystallites have the shape of truncated hexagonal bipyramids occasionally combined with the facets of a hexagonal prism. Most projections of such nanoparticles are nearly spherical under limited resolution as reported reported by Nielsen et al.[54] Elongated particles are expected to grow preferentially along the hcp *c*-axis of metallic ruthenium. We assume that they grow either along micropores (position γ in Figure 12, generally oriented in the [001] direction of the graphite, i.e. perpendicular to graphene layers) or along steps of graphene stacks on top of the graphite substrate (position α in Figure 12, *c*-axis of the metallic ruthenium perpendicular to the [001] direction of the graphene layers). Particles at position α in Figure 12 would explain the spread toward the *b*-axis in Figure 11. Not only the 'flattest' side touches the carbon support but also the 'next flattest' side, which sticks to the step of a stack of graphene layers. Particles that nucleate on top of micropore entries (position β in Figure 12) presumably form tabular ellipsoids by interaction of the (001) ruthenium facet with the graphene surface (epitaxial orientation).

The two-thirds of the ruthenium surface that touch the carbon support are also important since electrons have to be conducted from the carbon support to the ruthenium particle during catalysis in the fuel cell. The larger the contact area of the ruthenium particles to the carbon support, the higher is the conductance. We therefore expect the quantity Σ (the ratio of uncovered to total ruthenium surface) to possess an optimal value. If Σ is close to 0, the amount of uncovered ruthenium surface is low and limits catalytic activity, if Σ is close to 1, catalytic activity is limited due to insufficient conduction of electrons. Further experiments would be necessary to find out if $\Sigma = 0.36$ is close to the optimal value.

The ruthenium particle size distribution, assuming spherical symmetry, yields two diameters, the larger one at 2.8 nm with a variance of 1 nm. This result is comparable to the diameters evaluated by other methods: ASAXS[11]: 2.5 nm; XRD[11]: 2.2 nm; BF-TEM: 3 ± 1 nm. If only one Gaussian function (as for ASAXS and XRD) is fitted to the size distribution in Figure 4 the resulting mean diameter is about 2.5 nm. We explain the slightly higher estimate from TEM images by the actual deviation from spherical symmetry and the fact that isotropically oriented ellipsoidal particles generally appear bigger in a projection than the diameter estimated by an equal volume approach (as in Figure 4). In addition, particle selection by a scientist tends to lead to a choice of larger particles since smaller ones are more easily overlooked.

As any deviation of the ruthenium particles from spherical shape increases their surface-to-volume ratio, more surface is available for catalysis without an increase in material. The result is a more effective catalyst at the same material costs.

Particle shape analysis based on an approximation by ellipsoids shows that most particles (about 40% of 5700) have an undefined shape, i.e. neither prolate, oblate nor spherical. However, there are about twice as many prolate particles as oblate particles (prolate:oblate $\sim$ 2:1). This ratio is not affected much by the separation procedure (without separation it is 936:422) nor is the number of spherical particles increased significantly (412 before and 676 after separation). The shape of the ruthenium particles can be an indicator for preferential growth directions that can lead to differently sized and oriented facets. These preferential growth directions can be along edges of graphene layers on the outer surface or along pores of the support material (see Figure 12). Metallic hcp-Ru nanoparticles usually expose surfaces with different crystallographic orientation to the chemical reactants, likely featuring different catalytic activity depending on the size and orientation of the facets. Therefore, the ratio between prolate and oblate nanoparticles should be considered as one factor influencing the overall catalytic activity.

The ruthenium particle representations are expected to be affected by the 'missing wedge'[61] which causes an artificial elongation of the ruthenium particle representation. This will result in a tendency toward prolate ellipsoids in the shape analysis. Therefore, the actual ratio of prolate to oblate-shaped

particles will be more balanced than 2:1 (result from section 3.5). However, an actual deviation from spherical symmetry is definitely present due to the significant number of oblate particles. The effect of the missing wedge on spherical particles would only lead to prolate particle representations. Additionally, the fact that in most cases the *a*-axis of the ellipsoid is aligned parallel to the local surface normal (see section 3.8) rules out a significant effect of the missing wedge in the DIRECTT reconstruction. An elongation of the particles caused by the missing wedge would not be isotropic but only along one global axis which is in conflict with the result obtained by the local alignment analysis section (section 3.8) since the orientation of the local carbon surface normal can be expected to be isotropic.

5. CONCLUSIONS

We have demonstrated that TEM tomography can provide a quantitative structure analysis of catalytically active ruthenium nanoparticles supported by carbon. The size distribution of the ruthenium particles is bimodal for the investigated sample type. Particles from the smaller mode are formed preferentially within the more amorphous parts of the support, whereas larger particles are formed on the outer surface of the support. Fitting ellipsoids to the individual particles reveals that most particles are not spherical and the ratio of prolate to oblate particle numbers is about 2:1. The analysis of the alignment of the ruthenium particles with respect to the local support surface suggests that prolate particles presumably form along the edges of graphene sheets on the support or grow along pores. One factor influencing the overall catalytic activity is the ratio between prolate and oblate nanoparticles since it can indicate preferential growth directions which lead to differently sized facets. Thus, TEM tomography has proven to yield valuable information about the distinct nanostructure of different classes of catalytically active particles in general. Their individual contribution to the overall catalytic activity should be considered in further investigations to optimize the oxygen reduction performance of, e.g. carbon-supported selenium modified ruthenium catalysts ($RuSe_x/C$).

AUTHOR INFORMATION

Corresponding Author

*roman.grothausmann@helmholtz-berlin.de

6. ACKNOWLEDGMENT

We thank Dorothea Alber and Gregor Bukalis (HZB, NP-A2) for the NAA of the samples and Iris Herrmann-Geppert (HZB, E-I6) for the chemical characterizations of the samples.

ADDITIONAL NOTE

[a] The Otsu algorithm assumes that the image to be thresholded contains two classes of pixels (e.g., foreground and background) then calculates the optimum threshold separating those two classes so that their combined spread (intraclass variance) is minimal.

[b] This is a quantity different from the 'local catalyst loading' as reported in e.g. ref 52 where the mass of catalyst per support surface area is evaluated. There is no distinction between total and uncovered catalyst surface in the 'local catalyst loading'.

[c] Using the density of Ru: ρ_{Ru} = 12.37 g/cm^3 and a density of graphite: ρ_C = 2.25 g/cm^3.[51] V_{op} and the density of graphite are used because the density of graphite varies less than that of amorphous carbon which would be needed with V_{cp}.

[d] The stereographic projection causes less length/area distortion in the projected region than an orthographic projection would.

[e] Using the density of Ru: ρ_{Ru} = 12.37 g/cm^3 and the density of graphite ρ_C ranging from 2.0 g/cm^3 to 2.5 g/cm^3. The density of graphite is used because the pore volume is not included in the ratio calculation from the tomogram measurements.

REFERENCES

(1) Srinivasan, S.; Ticianelli, E.; Derouin, C.; Redondo, A. *J. Power Sources* **1988**, *22*, 359–375.
(2) Alonso-Vante, N.; Tributsch, H.; Solorza-Feria, O. *Electrochim. Acta* **1995**, *40*, 567–576.
(3) Trapp, V.; Christensen, P.; Hamnett, A. *J. Chem. Soc., Faraday Trans.* **1996**, *92*, 4311–4319.
(4) Rodríguez, F. J.; Sebastian, P. J.; Solorza, O.; Pérez, R. *Int. J. Hydrogen Energy* **1998**, *23*, 1031–1035.
(5) Zehl, G.; Bogdanoff, P.; Dorbandt, I.; Fiechter, S.; Wippermann, K.; Hartnig, C. *J. Appl. Electrochem.* **2007**, *37*, 1475–1484.
(6) Wippermann, K.; Richter, B.; Klafki, K.; Mergel, J.; Zehl, G.; Dorbandt, I.; Bogdanoff, P.; Fiechter, S.; Kaytakoglu, S. *J. Appl. Electrochem.* **2007**, *37*, 1399–1411.
(7) Papageorgopoulos, D. C.; Liu, F.; Conrad, O. *Electrochim. Acta* **2007**, *52*, 4982–4986.
(8) Comyns, A. E., Ed. *Focus on Catalysts*; 2007, 10.1016/S1351-4180(07)70248-9.
(9) Alonso-Vante, N. *Fuel Cells* **2006**, *6*, 182–189.
(10) Cao, D.; Wieckowski, A.; Inukai, J.; Alonso-Vante, N. *J. Electrochem. Soc.* **2006**, *153*, A869–A874.
(11) Zehl, G.; Schmithals, G.; Hoell, A.; Haas, S.; Hartnig, C.; Dorbandt, I.; Bogdanoff, P.; Fiechter, S. *Angew. Chem., Int. Ed.* **2007**, *46*, 7311–7314.
(12) Fiechter, S.; Dorbandt, I.; Bogdanoff, P.; Zehl, G.; Schulenburg, H.; Tributsch, H. *J. Phys. Chem. C* **2007**, *111*, 477–487.
(13) Bartram, S. F. In *Handbook of X-Rays*; Kaelble, E. F., Ed.; McGraw-Hill: New York, 1967; Chapter 17, pp 17.1−17.18.
(14) Frank, J. *Electron Tomography: Methods for Three-Dimensional Visualization of Structures in the Cell*, 2nd ed.; Springer: Berlin, 2006; p 455.
(15) Banhart, J., Ed. *Advanced Tomographic Methods in Materials Research and Engineering*; Oxford University Press: New York, 2008; pp 1−480.
(16) Kübel, C.; Voigt, A.; Schoenmakers, R.; Otten, M.; Su, D.; Lee, T.-C.; Carlsson, A.; Bradley, J. *Microsc. Microanal.* **2005**, *11*, 378–400.
(17) Friedrich, H.; Sietsma, J. R. A.; de Jongh, P. E.; Verkleij, A. J.; de Jong, K. P. *J. Am. Chem. Soc.* **2007**, *129*, 10249–10254.
(18) Friedrich, H.; de Jongh, P. E.; Verkleij, A. J.; de Jong, K. P. *Chem. Rev.* **2009**, *109*, 1613–1629.
(19) Midgley, P. A.; Dunin-Borkowski, R. R. *Nat. Mater.* **2009**, 271–280.
(20) Midgley, P. A.; Weyland, M.; Thomas, J. M.; Gai, P. L.; Boyes, E. D. *Angew. Chem.* **2002**, *114*, 3804–3807.
(21) Weyland, M.; Midgley, P. A.; Thomas, J. M. *J. Phys. Chem. B* **2001**, *105*, 7882–7886.
(22) Hata, S.; Kimura, K.; Gao, H.; Matsumura, S.; Doi, M.; Moritani, T.; Barnard, J. S.; Tong, J. R.; Sharp, J. H.; Midgley, P. A. *Adv. Mater.* **2008**, *20*, 1905–1909.
(23) Rösner, H.; Scherer, T.; Wilde, G. *Scr. Mater.* **2009**, *60*, 168–170.
(24) Gontard, L. C.; Dunin-Borkowski, R. E.; Chong, R. K. K.; Ozkaya, D.; Midgley, P. A. *J. Phys.: Conf. Ser.* **2006**, *26*, 203–206.
(25) Shirai, M.; Tsumori, K.; Kutsuwada, M.; Yasuda, K.; Matsumura, S. *Nucl. Instrum. Methods Phys. Res., Sect. B* **2009**, *267*, 1787–1791.

(26) Rösner, H.; Parida, S.; Kramer, D.; Volkert, C. A.; Weissmuller, J. *Adv. Eng. Mater.* **2007**, *9*, 535–541.
(27) Friedrich, H.; Guo, S.; de Jongh, P. E.; Pan, X.; Bao, X.; de Jong, K. P. *ChemSusChem* **2011**, *4* (7), 957–963.
(28) Kübel, C.; Niemeyer, D.; Cieslinski, R.; Rozeveld, S. *Material Science Forum*, THERMEC 2009, 6th International Conference on Processing & Manufacturing of Advanced Materials. Chandra, T., Wanderka, N., Reimers, W., Ionescu, M., Eds.; 2010; Vol. 638−642, pp 2517−2522.
(29) Ward, E. P. W.; Yates, T. J. V.; Fernandez, J. J.; Vaughan, D. E. W.; Midgley, P. A. *J. Phys. Chem. C* **2007**, *111*, 11501–11505.
(30) Grothausmann, R.; Manke, I.; Zehl, G.; Dorbandt, I.; Bogdanoff, P.; Fiechter, S.; Hentschel, M. P.; Lange, A.; Kupsch, A.; Hilger, A.; Banhart, J. *MP Mater. Test.* **2010**, *52*, 706–711.
(31) Nagabhushana, K. S.; Dinjus, E.; Bonnemann, H.; Zaikovskii, V.; Hartnig, C.; Zehl, G.; Dorbandt, I.; Fiechter, S.; Bogdanoff, P. *J. Appl. Electrochem.* **2007**, *37*, 1515–1522.
(32) Lange, A.; Hentschel, M. P.; Kupsch, A. *MP Mater. Test.* **2008**, *50*, 272–277.
(33) Vulcan XC-72R, Cabot Corporation, 2002.
(34) Brunauer, S.; Emmett, P. H.; Teller, E. *J. Am. Chem. Soc.* **1938**, *60*, 309–319.
(35) Barrett, E. P.; Joyner, L. G.; Halenda, P. P. *J. Am. Chem. Soc.* **1951**, *73*, 373–380.
(36) Lippens, B. C.; de Boer, J. H. *J. Catal.* **1965**, *4*, 319–323.
(37) Zehl, G.; Dorbandt, I.; Schmithals, G.; Radnik, J.; Wippermann, K.; Richter, B.; Bogdanoff, P.; Fiechter, S. *ECS Trans.* **2006**, *3*, 1261–1270.
(38) Koster, A.; van den Bos, A.; van der Mast, K. *Ultramicroscopy* **1987**, *21*, 209–222.
(39) Koster, A.; de Ruijter, W.; van den Bos, A.; van der Mast, K. *Ultramicroscopy* **1989**, *27*, 251–272.
(40) Kremer, J. R.; Mastronarde, D. N.; McIntosh, J. R. *J. Struct. Biol.* **1996**, *116*, 71–76.
(41) Lange, A.; Kupsch, A.; Hentschel, M. P.; Manke, I.; Kardjilov, N.; Arlt, T.; Grothausmann, R. *J. Power Sources* **2011**, *196*, 5293–5298.
(42) Hentschel, M. P.; Lange, A.; Kupsch, A.; Müller, B. R. *MP Mater. Test.* **2010**, *52*, 668–675.
(43) Otsu, N. *IEEE Trans. Syst., Man Cybernet.* **1979**, *9*, 62–66.
(44) ITK development team, *ITK*, open source, 3.18, http://www.itk.org.
(45) VTK development team, *VTK*, open source, 5.4; http://www.vtk.org.
(46) Eaton, J. W.; *GNU Octave*, open source, 3.0.5; http://www.gnu.org/software/octave.
(47) Kelley, W. C. *gnuplot*, open source, 4.4; 2010; http://gnuplot.sourceforge.net/docs_4.4/gnuplot.pdf.
(48) *Blender*, open source, 2.49; Blender Foundation: Amsterdam; http://www.blender.org.
(49) Beare, R.; Lehmann, G. *Insight J.* **2006**, *92*, 1–24.
(50) Soille, P. *Morphological Image Analysis: Principles and Applications*, 2nd ed.; Springer: New York, 2004; p 391.
(51) Wissler, M. *J. Power Sources* **2006**, *156*, 142–150.
(52) Midgley, P. A.; Thomas, J. M.; Laffont, L.; Weyland, M.; Raja, R.; Johnson, B. F. G.; Khimyak, T. *J. Phys. Chem. B* **2004**, *108*, 4590–4592.
(53) Ziegel, J.; Kiderlen, M. *Image Vision Comput.* **2010**, *28*, 64–77.
(54) Nielsen, R. M.; Murphy, S.; Strebel, C.; Johansson, M.; Chorkendorff, I.; Nielsen, J. H. *J. Nanopart. Res.* **2010**, *12*, 1249–1262.
(55) Lehmann, G. *Insight J.* **2008**, *176*, 1–34.
(56) Padfield, D.; Miller, J. *Insight J.* **2008**, *301*, 1–13.
(57) Lorensen, W. E.; Cline, H. E. *Comput. Graphics* **1987**, *21*, 163–169.
(58) Schroeder, W. J.Martin, K. M.Lorensen, W. E. *The VTK User's Guide*, 11th ed.; Kitware, Inc.: Clifton Park, NY, USA, 2010; pp 1−528.
(59) Kinoshita, K. *Carbon: Electrochemical and Physicochemical Properties*; Wiley & Sons: New York, 1988; pp 1−560.
(60) Rouquerol, J.; Avnir, D.; Fairbridge, C. W.; Everett, D. H.; Haynes, J. M.; Pernicone, N.; Ramsay, J. D. F.; Sing, K. S. W.; Unger, K. K. *Pure Appl. Chem.* **1994**, *66*, 1739–1758.
(61) Radermacher, M. *J. Electron Microsc. Tech.* **1988**, *9*, 359–394.